?RASONIC IMAGING 12, 245-267 (1990)

PARAMETRIC ULTRASOUND IMAGING FROM BACKSCATTER COEFFICIENT MEASUREMENTS: IMAGE FORMATION AND INTERPRETATION

Michael F. Insana and Timothy J. Hall

Department of Diagnostic Radiology
University of Kansas Medical Center
Kansas City, KS 66103

A broadband method for measuring backscatter coefficients σ_b and other acoustic parameters is described. From the σ_b measurements, using a commercially-available imaging system, four high-resolution parametric ultrasound images are formed in a C-scan image plane. Scatterer size images are computed from the frequency dependence of σ_b and a correlation model function that describes the structure and elastic properties of the medium. Scattering strength images are computed from the absolute magnitude of σ_b. Chi-square images are generated to display how well the correlation model represents the interrogated medium. Integrated backscatter coefficient images are formed over the transducer bandwidth. All four images are generated simultaneously and compared with the corresponding B-mode image. Test samples with known physical properties were used to demonstrate experimentally that accurate parametric images are possible if an accurate correlation model is used. Local variations in attenuation, the center frequency and bandwidth of the transducer, and the distribution of scatterer sizes greatly influence the accuracy of estimates and the appearance of the image, thus demonstrating the importance of these factors in parametric image interpretation.

Key words: Backscatter coefficient; correlation function; parametric imaging; scatterer size; scattering strength; spectral analysis; ultrasound.

1 INTRODUCTION

It is well known that the magnitude and frequency dependences of an acoustic echo signal spectrum are closely related to structural and elastic properties of the interacting medium — properties such as the size, shape, number, and organization of scattering sites. Because there are a large number of properties, and because the properties

0161-7346/90 $3.00

are interdependent, it is difficult to solve the general inverse scattering problem, *i.e.*, to extract accurate estimates of individual properties from the echo signal without simplifying assumptions.

Our approach to scattering-media characterization has been to estimate the *average* size and *net* scattering strength of structures by assuming, or measuring independently, the shape, organization, and essential elastic properties of scatterers in the medium [1]. Such prior information is incorporated into the analysis by introducing a correlation model. A correlation model relates properties of the medium at one spatial location to those at surrounding locations. When the correlation model is an accurate representation of the medium, the average size and scattering strength of structures may be determined. In practice, however, a correlation model is an approximation, and its fidelity to the data varies with experimental factors such as the center frequency and bandwidth of the interrogating pulse.

The most accurate measurements are obtained when the product of the wavenumber and the scatterer radius (ka) is between 0.5 and 1.2. In this range, the size of the scatterer is the principal factor determining the frequency dependence of ultrasonic backscatter. At very small values of ka (the Rayleigh scattering region), the noise in the spectral estimate is much greater than the changes due to the scatterer structure and measurement sensitivity is lost. At very large values of ka, properties of the medium other than size dominate the backscatter spectrum. Consequently, accurate scatterer size measurements at large ka requires that the medium be well characterized in all respects — a requirement that excludes many biological tissues. Biological tissues often contain structures of many sizes. While it can be difficult, if not impossible, to optimize the interrogation frequency for all tissue structures simultaneously, it may be possible to interpret the results and extract diagnostic information.

In this paper, we show how scatterer size estimates depend on the amount of prior information (correlation model), variations in attenuation, the interrogation frequency (ka), and the distribution of scatterer sizes. In particular, we examine how these factors affect parametric images. Unlike a B-mode image, where the echo amplitude is displayed, a parametric image displays the individual properties of the medium that determine the echo signal. A parametric image is most useful when it *quantitatively* represents physical properties of the medium. It is therefore essential to determine the experimental conditions where these properties can be accurately measured. For example, an inappropriate choice of transducer frequency or correlation model can mean a loss of both measurement accuracy and target detectability in a parametric image. Examination of these issues is an important step toward meaningful measurements in biological tissues.

2 METHODS AND MATERIALS

2.1 Backscatter coefficient estimation

Four parametric images are formed from each set of recorded data. Three of the parameters are derived from estimates of the backscatter coefficient σ_b, defined as the differential scattering cross section per unit solid angle at 180°, per unit volume. The fourth parameter is a measure of how well the correlation model represents the data. The analysis for estimating backscatter coefficients from echo signals was given previously [1] , and is summarized below.

Backscatter coefficients are estimated from a normalized power spectral density of the echo signal using the equation

$$\sigma_b(f) = \frac{1.45R_1^2}{A_0\Delta z} W(f), \tag{1}$$

where f is frequency in MHz, A_0 is the area of the transducer aperture, Δz is the axial length of the range gated volume, and R_1 is the on-axis distance between the transducer and the proximal surface of the gated volume. $W(f)$ is the average power spectral density of backscattered echo signals, divided by that from a reference signal, and is given by

$$W(f) = \frac{1}{N_l} \sum_{l=1}^{N_l} |S_l(f, Z_l)|^2 \tag{2}$$

and

$$|S_l(f, Z_l)|^2 = \left(\frac{\gamma'}{2}\right)^2 \frac{|S_m(k, Z_l)|^2}{|S_0(k, Z_l)|^2} e^{-4(\alpha_m - \alpha_0)(R_1 + \Delta z/2)}. \tag{3}$$

S_m is the Fourier transform of the sample echo signal, S_0 is the Fourier transform of the reference echo signal (measured using a planar reflecting surface), and $|\ |^2$ represents the squared modulus of the quantity. α_m and α_0 are the attenuation coefficients for the sample and reference media, respectively, N_l is the number of gated waveform segments of duration $Z_l\,\mu$s, and γ' is the amplitude reflection coefficient. ($\gamma' \simeq 0.37$ for plexiglas in distilled water at 22°C .)

The above equations describe a broadband substitution method for estimating σ_b using a weakly-focused transducer when the gated sample volume is placed near the radius of curvature of the transducer. The surface of the planar reference reflector is positioned at the radius of curvature, $R_1 + \Delta z/2$ from the transducer surface, and perpendicular to the beam axis.

When computing parametric images, we allowed for the option of forming images of σ_b at a specified frequency or integrating σ_b over a band of frequencies to form integrated backscatter coefficient *(IBC)* images. Each pixel in an *IBC* image is computed using the equation $\frac{1}{N_i}\sum_{i=1}^{N_i} \sigma_{b,i}$, where N_i is the number of frequencies in the working bandwidth, *e.g.*, the 12 dB bandwidth, of the transducer.

2.2 Scatterer size estimation

We assume that the medium to be characterized is fluid-like with spherically-symmetric inhomogeneities that scatter sound. If the inhomogeneities are discrete, the term scatterer size, D, refers to their average diameter; if the inhomogeneities are continuously varying functions of position, then D refers to the average correlation length. [Correlation functions and correlation lengths are discussed by Morse and Ingard [2], Sections 7.2 and 8.1 and Chernov [3], Chapter 1.]

The structure and elastic properties of the inhomogeneities determine how the backscatter coefficient changes with frequency. Scatterers are discrete or continuously varying; they are characterized by their size, shape, and orientation; they possess elastic

properties that may or may not support shear wave propagation; and they are regularly positioned, randomly positioned, or somewhere in between. In this paper, we restrict ourselves to measurements using well-defined test media for which all of the properties above that determine the backscatter coefficient are known. Consequently, correlation models may be computed based on that information to study changes in the frequency dependence of σ_b that are due exclusively to the size of the scatterer.

Instead of calculating correlation functions directly, we compute a function that is proportional to the Fourier transform of the correlation function — the acoustic intensity form factor F (Ref. [1]). The form factor describes changes in the backscatter coefficient as a function of frequency, and, in general, is a function of all the structural and elastic properties listed above. In the special case of randomly-positioned spherical scatterers, where all the properties are known except for size, F is only a function of frequency and sphere diameter D, and the backscatter coefficient for incoherent scattering may be written as [1]

$$\sigma_b(f) = C\, f^4\, D^6\, \bar{n}\gamma_0^2\, F(f, D). \tag{4}$$

The constant C is equal to $(\pi^4/36c^4)$ and c is the speed of sound in the medium. The product $\bar{n}\gamma_0^2$ is the scattering strength described in Section 2.3. In the long-wavelength limit where $\lambda \gg \pi D\,(i.e., ka \ll 1), F(f, D) \simeq 1$ and Eq. (4) reduces to the backscatter coefficient for Rayleigh scattering:

$$\sigma_0(f) = C\, f^4\, D^6\, \bar{n}\gamma_0^2\,. \tag{5}$$

In this formulation, any deviation of the frequency dependence of $\sigma_b(f)$ from f^4 is attributed to the form factor, which in turn depends on the scatterer size. We define F by the ratio

$$F(f, D) = \frac{\sigma_b}{\sigma_0}. \tag{6}$$

Form factors are *modeled* by calculating backscatter coefficients using prior information about the scattering medium. Two models are emphasized in this paper; both assume discrete spherical scatterers made of solid materials that are suspended in a fluid. In the first model, F_1, the function σ_b is calculated using the theoretical formulation for acoustic scattering from spheres derived by Faran [4] as described previously [1] . The accuracy of Faran's formulation for predicting the scattered pressure is well established in the literature. We have shown experimentally that for well-defined test media, such as glass or polystyrene spheres randomly positioned in agar, the frequency dependence of backscatter, and hence scatterer size, was correctly predicted by F_1. (For example, see figure 5 in [1]) Because of the complexity of the Faran scattering equations, F_1 model functions are determined numerically.

In a second, more elementary model, which we call the spherical shell model, F_2, we assume the spheres are mechanically rigid, and ignore the propagation of pressure waves inside the spheres. This simplifying assumption allows for a closed-form solution given by

$$F_2(f, D) = (j_0(2\pi f D/c))^2, \tag{7}$$

where j_0 is a spherical Bessel function of the first kind, zero order. The spherical shell model accurately represents the frequency dependence of backscattering from the glass sphere-in-agar test media when $ka \leq 1.2$ (Ref. [1]).

Form factors are *measured* by estimating backscatter coefficients over the 12 dB bandwidth of the transducer using Eq. (1), dividing by f^4, and rescaling the result such that the extrapolated form factor value at zero frequency is one.

The average scatterer size is then estimated by comparing form factor model functions to that measured for the sample using a least-squares method. Two sets of model form factor functions are calculated and stored in a look-up table *(LUT)*: one set for F_1 and one set for F_2. Both sets contain functions that span a 5 to 250 μm range of sphere diameters. Having chosen either F_1 or F_2 for the analysis, the average scatterer size was determined by noting the diameter associated with the model function that fits the measured form factor $\hat{F}$ with the minimum averaged squared deviation (MASD). In practice, we find the MASD of the log-difference function $\log \hat{F} - \log F$. The deviation of the log difference has the desirable property of emphasizing the bias rather than the variance between the model and the data [5]. Also, the log-difference criterion gives equal weight to each frequency component; a linear difference criterion favors spectral components with high signal-to-noise over low signal-to-noise. With this technique, it was possible to estimate sphere diameters to within 10 percent of the known value using F_1 and 20 percent using F_2 (Ref. [1]). These results demonstrate the improved accuracy for size estimation that is possible when the more detailed model F_1 is used.

While forming scatterer size images, we concurrently computed chi-square (χ^2) images using the MASD values. The χ^2 image indicates how well the model function describes the data as a function of position in the medium. χ^2 is given by the sum [6]

$$\chi^2 = \sum_{i=1}^{N_i} \frac{(\Delta \log F_i)^2}{var(\log \hat{F}_i)}, \tag{8}$$

where $\Delta \log F_i = \log \hat{F}_i - \log F_i$ at the ith frequency in the bandwidth and $var(\log \hat{F}_i)$ is the variance in the log form factor estimate at the same frequency. Bendat and Piersol [7] have shown that $var(\log \hat{F}_i) \simeq 1/N_l$, where N_l is the number of waveforms averaged to determine $\hat{F}$, and *not* the number of frequencies in the bandwidth N_i. The variance therefore is independent of frequency. Chi-square image values were computed using the equation

$$\chi^2 \simeq \frac{1}{N_l} \sum_{i=1}^{N_i} (\Delta \log F_i)^2. \tag{9}$$

2.3 Scattering strength estimation

The net scattering strength, $\bar{n}\gamma_0^2$, is defined as the product of the average number of scatterers per unit volume, $\bar{n}$, and the mean-square variation in acoustic impedence between a scatterer and the surrounding medium, γ_0^2. In terms of compressibility κ, density ρ, and speed of sound c,

$$\gamma_0^2 = \left(\frac{\Delta\kappa}{\kappa} - \frac{\Delta\rho}{\rho} \right)^2 \simeq 4 \left(\frac{\Delta(\rho c)}{\rho c} \right)^2. \tag{10}$$

In samples where all the scatterers have the same elastic properties, such as those used in this study, variations in $\bar{n}\gamma_0^2$ indicate variations in the average number density of scatterers $\bar{n}$.

The scattering strength is directly proportional to the backscatter coefficient, such that once the average scatterer size is estimated, the scattering strength is the only remaining unknown in Eq. (4). The procedure and equations for estimating $\bar{n}\gamma_0^2$ have been described [1].

2.4 B-mode images

A fifth image, the B-mode image, is also computed from the same set of rf echo signals. Each pixel in our B-mode image displays the mean-square echo signal within the range gate, *i.e.*, $\frac{1}{2N_i}\sum_{i=1}^{2N_i} x_i^2$, where there are $2N_i$ points in the range gate per waveform. (See Section 2.5 for details.)

We have considered two other options for computing B-mode images: the *rms* signal and the *peak* signal. Of the three, B-mode images derived from the mean-square signal provided the most direct comparison with parametric images computed from the backscatter coefficient. The rms value is proportional to the magnitude of the signal while the mean-square value and the backscatter coefficient are both proportional to the intensity of the signal. Diagnostically, magnitude and intensity echograms are similar, since the lesion signal-to-noise ratio, a measure of low-contrast detectability, is approximately equal for both images [8]. Images derived from the peak signal value were also generated and found to be very "noisy" compared to rms and mean-square echograms. Differences in noise levels are due to differences in the amount of data used to form the image. Each peak value has the uncertainty associated with a single point on the waveform, whereas the rms and mean-square values have uncertainties associated with an average of $2N_i$ points. The algorithm for computing B-mode and four parametric images is summarized in figure 1.

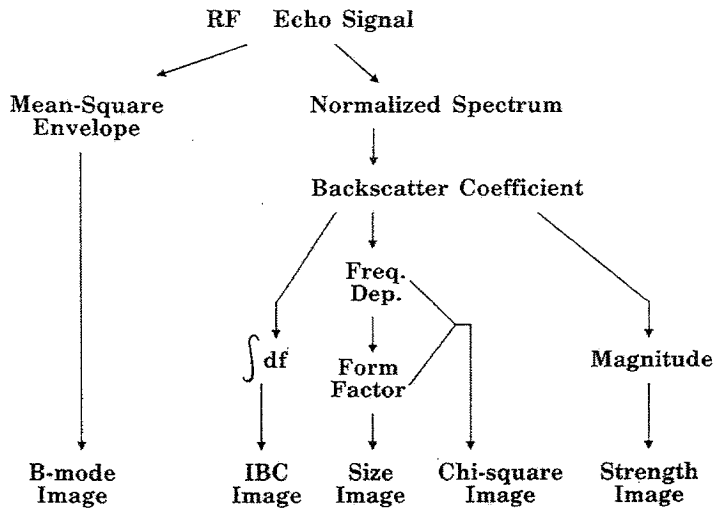

Fig.1 Diagram of the image formation process. A B-mode image and four parametric images are formed from each data set.

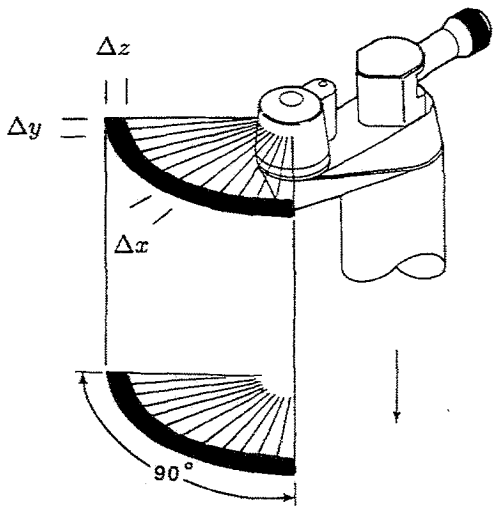

Fig.2 Illustration of C-scan data acquisition. Parameters are estimated from data recorded within the range gate, Δz. The horizontal image axis is in the scan plane of the mechanically-steered trans- ducer. The distance between waveforms is Δx. The transducer is translated in elevation a distance Δy to form the vertical axis of the image, *e.g.*, figure 7.

2.5 Image formation

In conventional B-scan ultrasonography, the axis of the transducer beam lies in the plane of the image (x, y). In C-scan imaging, the beam is perpendicular to the image plane as shown in figure 2. (We use the terms B-scan and C-scan to identify the image plane with respect to the beam axis. B-mode refers to the quantity imaged, *e.g.*, the echo signal amplitude or intensity: brightness.) The advantage of C-scan imaging is that data outside of the image plane, *i.e.*, along z, may be processed, thus preserving spatial resolution in the image plane and allowing the entire image to lie inside the focal zone of the transducer. Disadvantages include increased scan times (currently transducers that are mechanically or electronically steered in only one dimension are commercially available), partial-volume effects, and, for sector scans, a curved scan volume.

Data were acquired by one of the two C-scan techniques shown in figure 3. In one technique, an ATL Mark V (Bothell, WA) mechanical sector scanner provided the means for collecting data at 7.5 MHz. With each revolution of the rotating scan head, one scan plane (x, z) was recorded. The waveforms in each scan plane were analyzed along the z-axis (range direction) to produce one row of image data along the x-axis. At the center of the range gate, the distance along the x-axis between waveforms in the scan plane was 0.5 mm. Consequently, the transducer was then translated 0.5 mm along the y-axis before recording the next scan plane so that the pixels in the image plane were square. Since the operator had to move the transducer in only one dimension (along the y-axis), the total data acquisition time was 3 to 5 minutes for a typical image size of 40 mm x 60 mm. A reference signal was later recorded by stopping the rotation of the scan head to align the planar surface. Both sample and reference signals were recorded using only one of the three scanhead elements. The center frequency of that element was 7.0 MHz, the 12 dB bandwidth was 6.0 MHz, the nominal aperture diameter was 6 mm, and the focal length was 33 mm.

In the other technique, a broadband pulser/receiver and a single-element circular transducer were used to scan samples at 10 MHz. The sample was scanned by manually

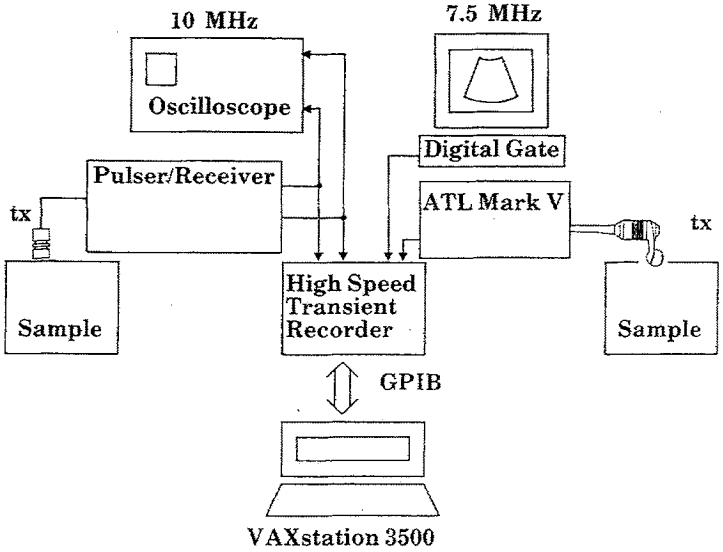

Fig.3 Block diagram of the 10 MHz and 7.5 MHz data acquisition systems.

translating the transducer in two dimensions using a rectilinear-scanning motion and 0.5 mm increments; it took several hours to manually scan a sample and collect data for a typical image. The center frequency of the transducer was 10.0 MHz, the 12 dB bandwidth was 12.5 MHz, the nominal aperture diameter was 19 mm, and the focal length was 53 mm. The 10 MHz technique was used to obtain high-frequency data with a very broad bandwidth not available with the scanner.

In both techniques, the maximum image format size was 128 x 128 pixels. One echo signal waveform was recorded for each pixel in the image. When the 7.5 MHz system was used, the digitization rate was 25 Msamples per second and the resolution was (nominally) 8 bits. When the 10 MHz system was used, the digitization rate was increased to 50 Msamples per second, at 8 bits. Range gated waveform segments, Δz, with durations between 5 mm and 15 mm were analyzed. Each waveform segment was first multiplied by a Hanning window before computing the Fourier transform using an FFT algorithm. From each echo spectrum, backscatter coefficients were computed at frequencies within the transducer bandwidth according to Eq. (1). Further analysis produced estimates of IBC, $D, \bar{n}\gamma_0^2$, and χ^2 as described above. Parameters were assigned gray-level values according to their magnitude and mapped into separate gray-scale parametric images. All data were reduced off-line and displayed using a VAXstation 3500.

2.6 Test samples

Two types of test samples were used in this study. The first type was a water-based agar material that contained randomly-positioned glass spheres (Duke Scientific Corporation, Palo Alto, CA). The distribution of sphere diameters was strongly peaked about the mean value so that a single particle size could be assumed, *i.e.*, standard deviations were less than 4 percent of the means. The density, longitudinal speed of

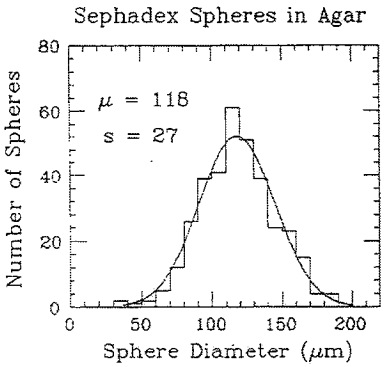

Fig.4 Histogram of sphere diameters in the Sephadex-in-agar test sample. The histo- gram was modeled using a normal pdf with parameters $\mu = 118$ μm and s = 27 μm.

sound, and Poisson's ratio for glass are 2.38 g/cm^3, 5570 m/s, and 0.21, respectively. The agar was taken to be fluid-like, the density was 1.00 g/cm^3, and the speed of sound was 1545 m/s.

The second type of test sample was a water-based agar material that contained randomly-positioned Sephadex filtration beads (Pharmacia Laboratory, Piscataway, NJ). Sephadex is an extremely hydrophilic gel prepared by cross-linking dextran with epichlorohydrin. We used the G-25 type Sephadex having a 20 to 80 μm dry bead diameter range. The Sephadex beads were soaked in distilled water for 14 hours before making the test sample. Thin sections of the Sephadex - agar material were examined under a light microscope to determine the diameter distribution. A histogram of the results is shown in figure 4. The histogram is approximated by a normal probability density function (pdf) with a mean diameter of 118 μm and a standard deviation of 27 μm. For the G-25 type Sephadex, the mean diameter of the wet beads in agar was approximately 2.4 times that of the dry beads. The bead diameter in the sample depended on the alcohol content of the agar and on the type and grade of the Sephadex. The agar was prepared from a solution of 10 percent n-propanol in water. We measured the density (1.10 ± 0.01 g/cm^3) and the longitudinal speed of sound (1601 ± 5 m/s) of a gravity-packed column of Sephadex in water, and estimated a Poisson's ratio of 0.4993.

The attenuation and speed of sound were measured for each test material using a standard through-transmission narrowband method. Average values are summarized in Table I.

Table I. Properties of the four agar test materials described in Section 3.

Scatterer Material	Sphere Diameter (μm)	No. per mm^3	Sound Speed (m/s)	Attenuation (dB/cm)
glass	41 ± 2	24.2	1540	0.17 $f^{1.4}$
glass	75 ± 3	3.0	1543	0.26 $f^{1.0}$
glass	105 ± 4	1.5	1547	0.26 $f^{1.1}$
Sephadex	118 ± 27 (wet)	14.3	1547	0.21 $f^{1.0}$

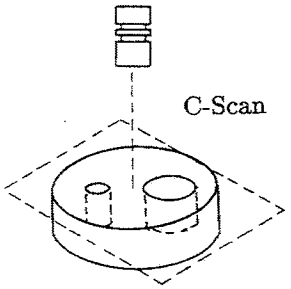

Fig.5 A diagram of a test sample and scan plane.

Each test sample was formed into a cylindrical shape that was 7.5 cm in diameter and 2.5 cm in height. Two cylindrical targets, 2.5 cm and 1.0 cm in diameter, were cut from each sample, as shown in figure 5. Interchanging these targets among the samples provided known object contrast for imaging.

3 EXPERIMENTAL RESULTS

3.1 Backscatter coefficient estimates

Backscatter coefficient estimates were compared with values predicted by theory [4] to verify the analysis summarized by Eqs. (1)–(3). Two examples are given in figure 6. Samples containing 41 μm diameter glass spheres in agar (a) and 105 μm diameter glass spheres in agar (b) were measured at 7.5 MHz using the sector scanner. In both

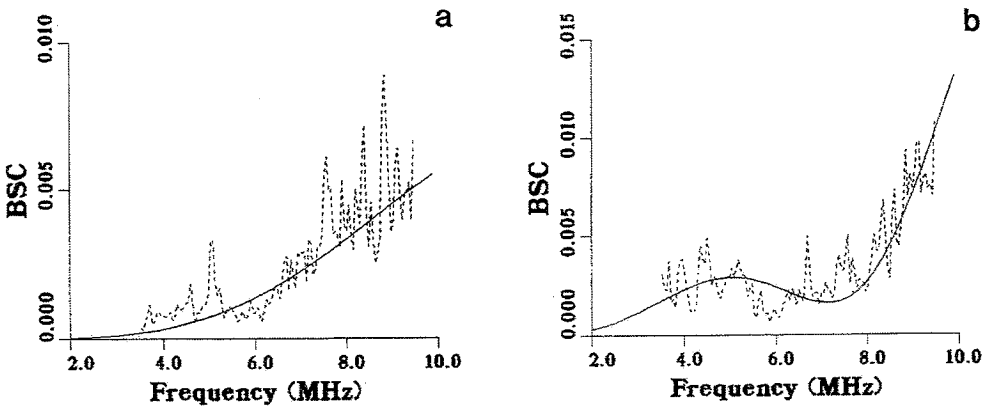

Fig.6 Backscatter coefficients for two glass micro- sphere-in-agar test samples. Dotted lines represent measurements and solid lines re- present theory [4]. The data in (a) were measured using a sample containing 41 μm diameter spheres and a density of 24.2 spheres per mm^3. The data in (b) were measured using a sample containing 105 μm diameter spheres and a number density of 1.46 spheres per mm^3.

examples, the spectra from twenty-five adjacent waveforms were averaged ($N_l = 25$), and the transducer was translated 0.5 mm between waveform recordings, *i.e.*, less than one-half aperture. Therefore we could not assume that the waveforms were independent. Each waveform was 20 μs in duration. In both cases, the measured and predicted values were in agreement.

3.2 Correlation models and attenuation

C-scan images of test sample A are displayed in figure 7. The large and small circular targets contain 41 μm diameter glass spheres in agar, a number density of 24.2 spheres per mm^3, and attenuation constants $\alpha = 0.17$ dB/cm MHz^m and $m = 1.4$. The background material contains 75 μm diameter spheres, a number density of 3.0 spheres

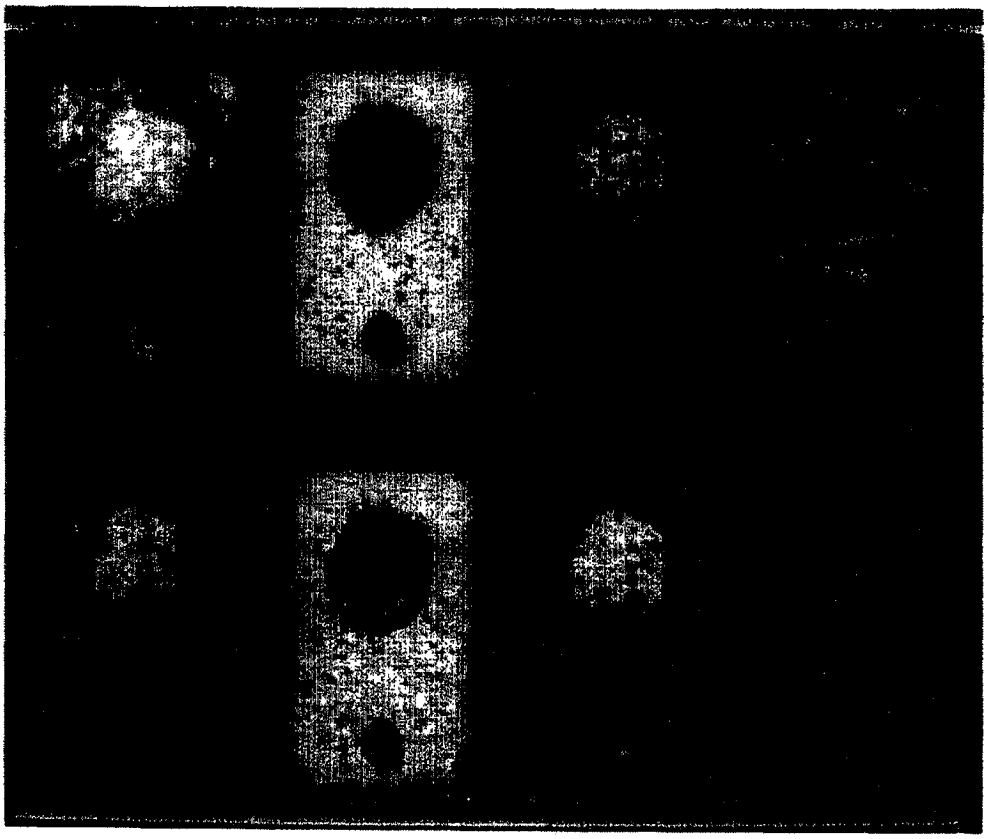

Fig.7 C-scan images of *test sample A* using a sector scanner at 7.5 MHz. (a) is a B-mode image and (e) is an *IBC* image. (b) and (f) are scatterer size images, (c) and (g) are scattering strength images, and (d) and (h) are χ^2 images. Images (b), (c), and (d) were formed using the spherical shell correlation model F_2, and images (f), (g), and (h) were formed using the model derived from theory F_1. See Section 3.2 for details.

per mm^3, $\alpha = 0.26$ dB/cm MHz^m and $m = 1.0$. Note that the attenuation constants for the target and nontarget materials are very different. All eight images were formed from one data set acquired using the 7.5 MHz sector scanner. Each image was scaled independently for display purposes only.

Image (a) is a B-mode image, (b) and (f) are scatterer size images, (c) and (g) are scattering strength images, (d) and (h) are chi-square images and (e) is an integrated backscatter coefficient image. The spherical shell model F_2 was used to compute parameters in images (b), (c), and (d), while the Faran-theory model F_1 was used in (f), (g), and (h). In the background, where the spheres were 75 μm in diameter, we measured 81 $\pm$ 6 μm using F_1 (image f) and 69 $\pm$ 5 μm using F_2 (image b). In the targets, where the spheres were 41 μm in diameter, we measured 61 $\pm$ 4 μm using F_1 and 58 $\pm$ 5 μm using F_2. The attenuation constants for the background were used to reduce all the data in the image; therefore, sphere diameters were accurately estimated in the background but not in the targets. An underestimation of the attenuation at higher frequencies corresponds to an overestimation of sphere sizes, as we showed previously [1] .

The ratio of target to nontarget scattering strengths was 8.1; our estimate was 4.2 $\pm$ 2.0. This discrepancy is consistent with the error in scatterer size, as discussed later in Section 4.

The χ^2 images, (d) and (h), have approximately the same average intensity and are uniform, indicating that both models F_1 and F_2 represent the small-scale structure of the media equally well, and that each model equivalently describes scatterers inside and outside the targets. In the target and background regions, $0.5 \leq ka \leq 1.2$ for most of the transducer's bandwidth. Therefore, the choice of model was of little importance, and the errors in parameter estimates can be explained entirely by errors in the attenuation constants.

Finally, the *IBC* image (e) is very similar in appearance to the B-mode image, except that the edges of the circular targets in the *IBC* image appear slightly sharper.

C-scan images of test sample B are displayed in figure 8. The targets contain 105 μm diameter glass spheres in agar, a number density of 1.46 spheres per mm^3, and attenuation constants $\alpha = 0.26$ dB/cm MHz^m and $m = 1.1$. The background is the same 75 μm material used in sample A.

Labels (a) through (h) in figure 8 correspond to those in figure 7 described above. In the background, where the spheres are 75 μm in diameter, we measured 83 $\pm$ 9 μm using F_1 (image f) and 69 $\pm$ 4 μm using F_2 (image b). In the targets, where the spheres are 105 μm in diameter, we measured 104 $\pm$ 13 μm using F_1 and 64 $\pm$ 6 μm using F_2. Attenuation was not a factor in these images because the attenuation constants inside and outside the targets were very similar. The choice of model, in this case, was very important, since ka for the target material was greater than 1.2 for most of the bandwidth. More prior information is needed to accurately describe scattering at high values of ka than at low values, and that information is more accurately provided by F_1 than F_2.

The breakdown of the F_2 model is also evident from the χ^2 images. The average χ^2 value is larger in the targets than in the background when the F_2 model is used (image d). Conversely, χ^2 values are uniformly low when the F_1 model is used (image h), since that model is valid throughout the image. Hence the sphere diameters throughout image (f) are accurately determined. Also, the ratio of target to nontarget scattering strength estimates was 0.49; our estimate was 0.60 $\pm$ 0.27 in image (g), where the model

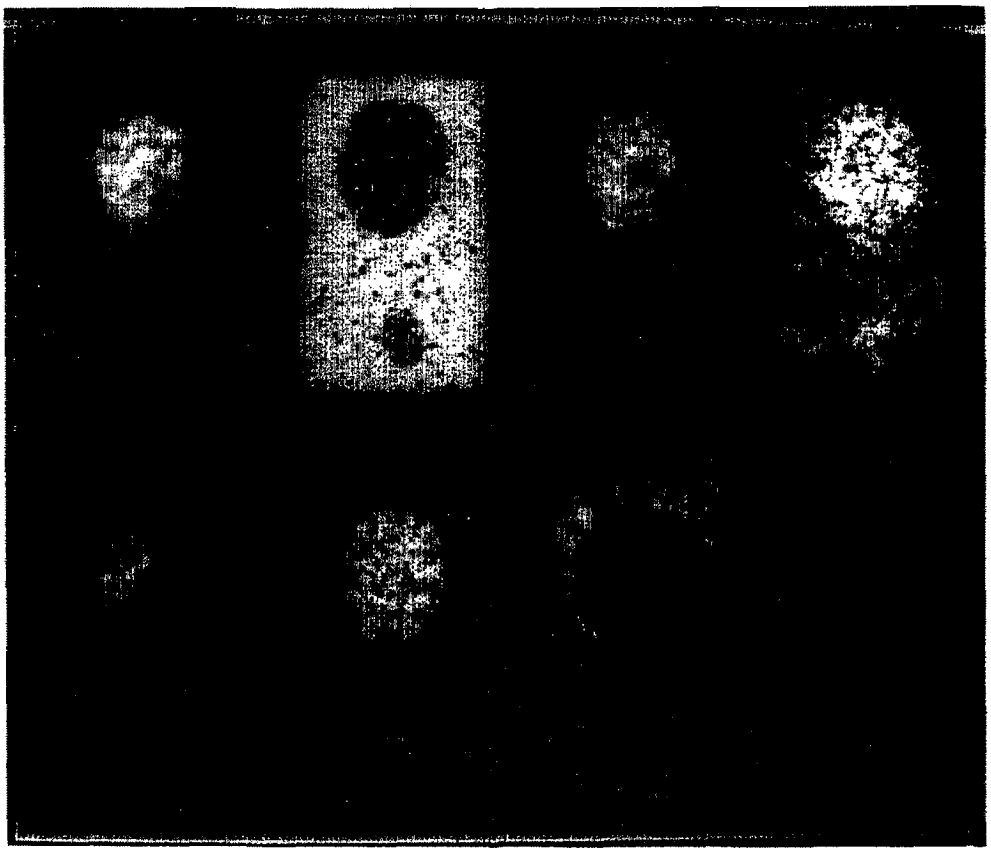

Fig.8 C-scan images of *test sample B* using a sector scanner at 7.5 MHz. (a) is a B-mode image and (e) is an *IBC* image. (b) and (f) are scatterer size images, (c) and (g) are scattering strength images, and (d) and (h) are χ^2 images. Images (b), (c), and (d) were formed using the spherical shell correlation model F_2, and images (f), (g), and (h) were formed using the model derived from theory F_1. See Section 3.2 for details.

F_1 was used to compute scatterer size. In summary, an accurate correlation model is necessary to accurately estimate the scatterer size and strength.

As in figure 7, the *IBC* image is very similar to the B-mode image, with the exception of the sharpness of edges on the circular targets.

3.3 Correlation model, center frequency, bandwidth

When studying correlation models, the first thing we noticed was that many of the models were very similar at small ka, but very different at large ka. For example in figure 9, the Faran model F_1 and the spherical shell model F_2 are compared with a form factor computed from a Gaussian correlation model (labeled G). (See Eq. (22) in [1]). At $ka \leq 1.2$, F_1 and F_2 are very similar, and therefore we were able

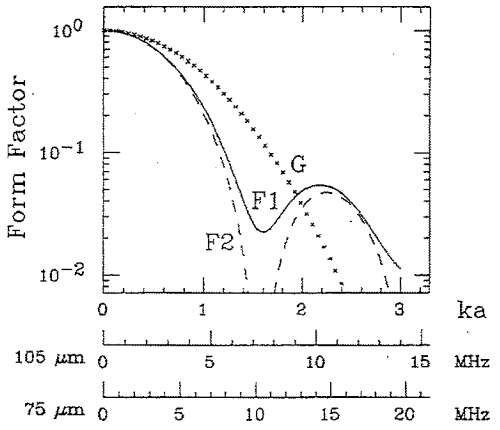

Fig.9 Three form factor models are compared. F_1 is derived from scattering theory for spheres [4], F_2 is the spherical shell model, and G is the Gaussian model (See Eq. (22) in [1]). The functions are plotted in ka and in frequency for the 105 μm and 75 μm diameter spheres.

to accurately measure scatterer sizes in this range with either model [1] . However, in the same range with the Gaussian correlation model, sphere sizes were consistently overestimated: to match the Faran model for a given size requires a Gaussian model of a much larger size. In that sense, the Gaussian model is inappropriate for sizing spheres. At $ka > 1.2$, the Gaussian model monotonically decreases, while F_1 and F_2 oscillate and ultimately diverge. Consequently, parameter estimates for each model can vary considerably depending on the center frequency and bandwidth of the transducer. This section summarizes our investigations into the measurements of scatterer size as a function of ka for the correlation models F_1 and F_2.

3.3.1 5 MHz bandwidth

Figure 10 is a display of scatterer size images using the spherical shell model F_2 and test sample B (105 μm glass spheres in targets, 75 μm glass spheres in background.) Data were acquired with the 10 MHz equipment described in Section 2.5 and figure 3. The spectrum's 12.5 MHz total bandwidth was partitioned into four overlapping segments: 2.5 to 7.5 MHz, 5.0 to 10.0 MHz, 7.5 to 12.5 MHz, and 10.0 to 15.0 MHz. Scatterer size images computed over these four frequency ranges resulted in figures 10a through 10d, respectively. One set of data was used to compute scatterer size estimates for a fixed working bandwidth (5 MHz), but four different center frequencies (5.0, 7.5, 10.0, 12.5 MHz). Distributions of D values measured from the data in the target and background regions are also displayed in figure 10. For each distribution, the total number of samples (pixels) was 1400. The F_1 and F_2 models may be compared at different frequencies by referring to figure 9.

$(ka)_{bkg} < 1.2$, $(ka)_{targ} \sim 1.2$

In the frequency range 2.5 to 7.5 MHz, figure 10a, $ka < 1.2$ for the background (75 μm spheres), the size distribution has a single peak, and the average D value is accurately estimated at $D_{bkg} = 74 \pm 17\mu$m. In the targets (105 μm spheres), $ka > 1.2$ for much of the bandwidth, and F_2 diverges from the more accurate Faran model F_1. Between $1.0 \leq ka \leq 1.4$, the F_2 model decreases faster with ka than the data

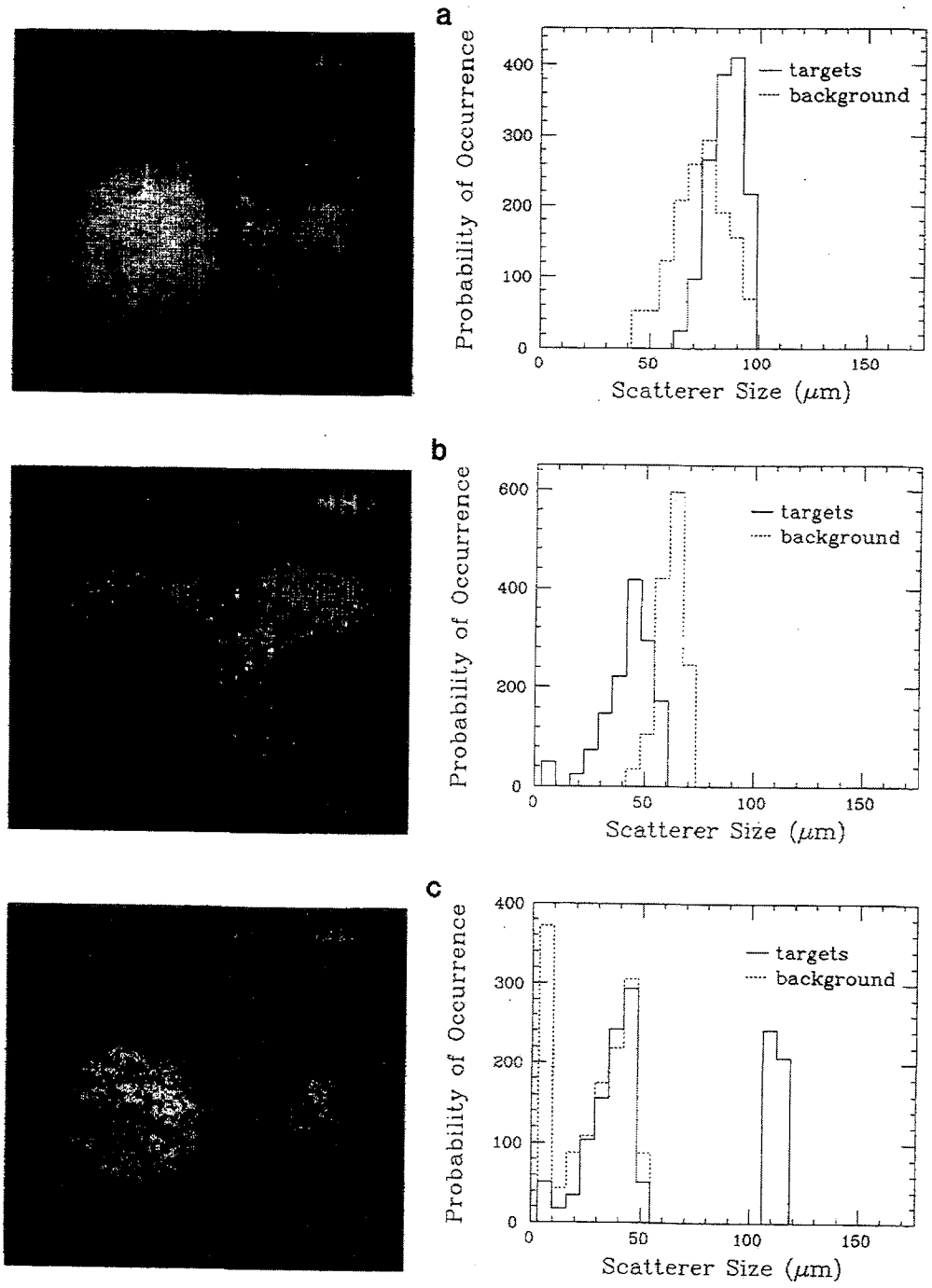

Fig.10 Images of scatterer size (left) and histo- grams of image values (right) for test sample B (105 μm glass spheres in targets, 75 μm glass spheres in background.) Size estimates were made using the spheri- cal shell model F_2. The working bandwidths were 2.5 to 7.5 MHz in (a), 5.0 to 10.0 MHz in (b), 7.5 to 12.5 MHz in (c), and 10.0 to 15.0 MHz in (d). See Section 3.3.1.

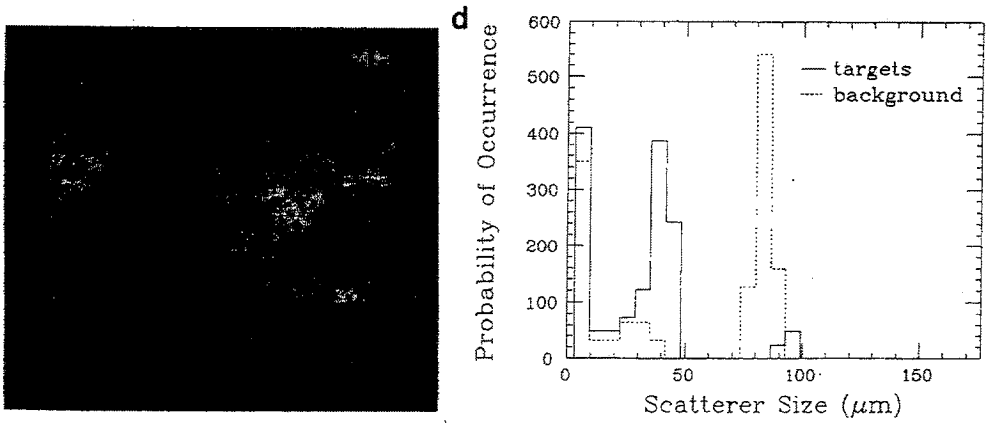

Fig.10 - Continued

(represented by F_1 in figure 9), and the average D value is biased low: $D_{targ} = 88 \pm 10\mu$m.

$(ka)_{bkg} \sim 1.2$, $(ka)_{targ} > 1.2$

In the frequency range 5.0 to 10.0 MHz, figure 10b, the average D estimate has decreased in both the background and target regions. The inability of the F_2 model to represent the scatterers in this range results in an underestimation of D, which is greater in the target regions. $D_{targ} = 49 \pm 24\mu$m and $D_{bkg} = 65 \pm 13\mu$m. As a result, the targets appear darker than the background in the image.

$(ka)_{bkg} > 1.2$, $(ka)_{targ} > 1.2$

In the frequency range 7.5 to 12.5 MHz, figure 10c, the distributions in the targets and background become bimodal. The background yields peaks around 40μm and 5μm. ($5\ \mu$m is the minimum size we selected in the LUT used to fit model functions to the data.) The peak at $5\ \mu$m results from fitting an inaccurate model function to noisy data. The $5\ \mu$m peak occurs in the background material, in this frequency range, when the analysis finds that a model corresponding to a very small sphere diameter — a very flat frequency dependence — gives the least-squares estimate.

Inside the target material, the analysis was not able to uniquely identify data as corresponding to the first or second lobe of the form factor model. Hence, when the scattering function oscillates as it does for spheres, there will be an ambiguity in D estimates, particularly when there is noise in the data. When the data fits the second lobe better than the first, the estimate is $112 \pm 7\mu$m — very close to the actual value of $105\ \mu$m. When the data fits a section of the first lobe with a similar frequency dependence, the estimate is $39 \pm 22\mu$m. Consequently, in both target and background regions, the image has a "salt and pepper" look, and the average target brightness is now greater than the background.

In the frequency range 10.0 to 15.0 MHz, figure 10d, the effects described above are also seen, except the relative number of pixels in each peak has changed, and the targets have once again changed polarity relative to the background.

3.3.2 12.5 MHz bandwidth

We have observed the same multiple peak behavior in sizing scatterers using the Faran model, F_1. This behavior can be expected whenever an oscillating model is being matched to noisy data. The most accurate size image was obtained using the F_1 model over the entire 12.5 MHz bandwidth (Fig. 11). Plotting the distribution of sizes for the entire image (9600 pixels) resulted in three peaks in figure 11a: 71 ± 6 μm, 104 ± 3 μm, and 245 ± 2 μm. The ratio of areas under the 71 μm and 104 μm peaks is 4.0 — exactly

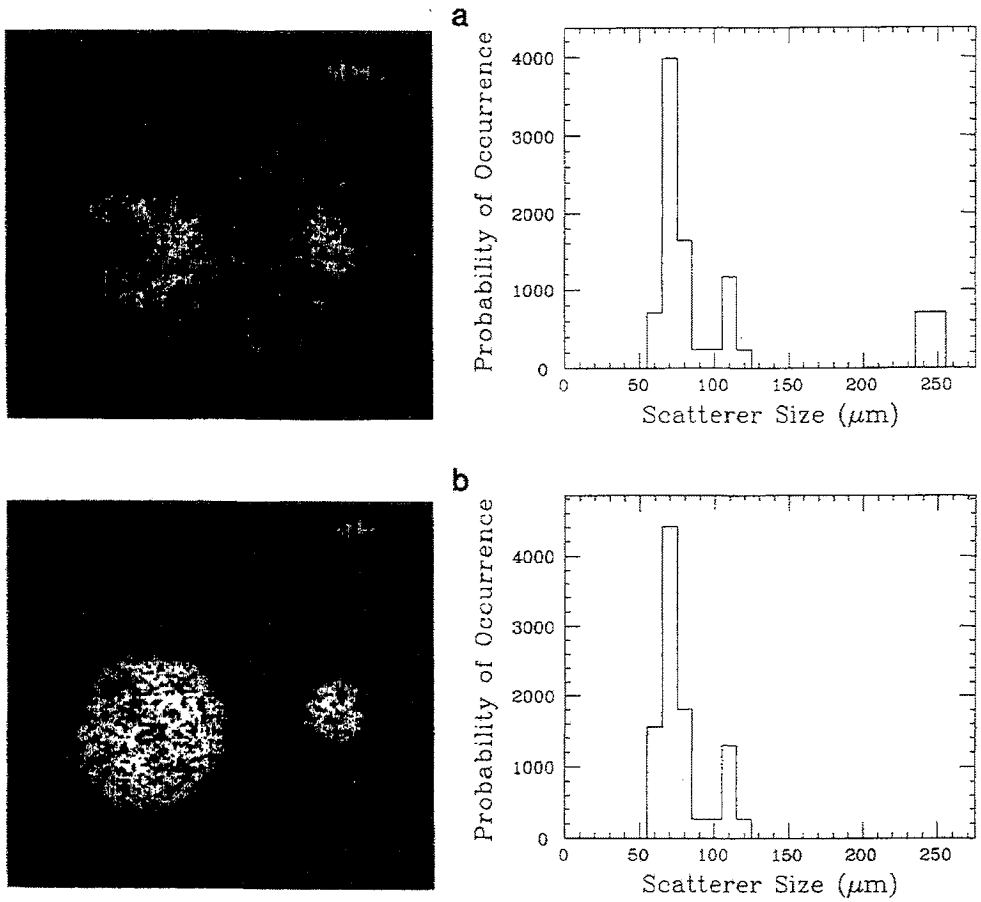

Fig.11 Scatterer size images for test sample B and histograms of entire images are displayed. The analysis includes form factors for sizes between 5 and 250 μm in (a) and 5 to 150 μm in (b). In both images the Faran-theory model, F_1, was used to estimate D and the working bandwidth was 2.5 to 15.0 MHz. The occurence of the 245 μm peak in the histogram of image (a) is an artifact that is removed by reducing the upper limit of form factors in the LUT as shown in (b). The ratios of areas under the 71 μm and 104 μm peaks are equal to the ratios of background to target areas. See Section 3.3.2.

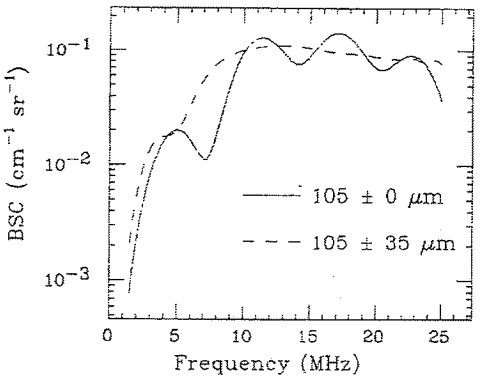

Fig.12 A comparison of two theoretical backscatter coefficient curves for glass spheres In one case, the modeled medium contains 105 μm diameter spheres only (solid line). In the other case, the modeled medium contains a normal distri- bution of sphere diameters about a 105 μm mean (dashed curve). The total number of spheres in both curves were equal.

the ratio of background pixels to target pixels. The small peak at 245 μm is an artifact of the noise in the spectral estimates. Form factor functions for large scatterers are more convoluted than those of small scatterers, and occationally the match between very large scatterer model functions and noisy spectra satisfies the MASD criterion, particularly with very broad bandwidth pulses as in figure 11a. The largest sphere size in the LUT was 250 μm. If in the analysis we reduce the upper limit to 150 μm, *i.e.*, make use of prior information, this artifact is eliminated as shown in figure 11b.

3.4 Broad scatterer-size distributions

In all the results described above, there was a narrow distribution of scattering sphere diameters about the mean. Since estimates of D strongly depend on the value of ka, scatterer size measurements for media with a broad size distribution were also investigated.

Size estimates were predicted for media with broad size distributions using computer simulations. Form factors were computed for each sphere diameter in a distribution, the resulting functions were weighted by the number fraction of spheres at that diameter, and all the contributions were summed. The Faran model F_1 was used to simulate these form factors. For example, in figure 12, the predicted backscatter coefficients for two media are plotted. In one plot, each sphere is exactly 105 μm in diameter; in the other plot, a distribution of diameters that follows a normal pdf with a mean of 105 μm and a standard deviation of 35 μm is used in the calculation. The average total backscatter coefficient for the second plot is given by the equation

$$\bar{\sigma}_b = \sum_{i=1}^{\infty} \frac{\bar{n}_i}{\bar{n}_T} \sigma_{b,i} \,, \tag{11}$$

where $\bar{n}_i$ is the number of spheres per unit volume having a diameter between D and $D+\Delta D$ and $\bar{n}_T = \sum_{i=1}^{\infty} \bar{n}_i$. With Eq. (11), we have assumed the scattering is incoherent and the spheres are randomly positioned. Because the backscatter coefficient depends on the diameter distribution, so do estimates of D and $\bar{n}\gamma_0^2$. Therefore, in general, the correlation model should include information about the distribution.

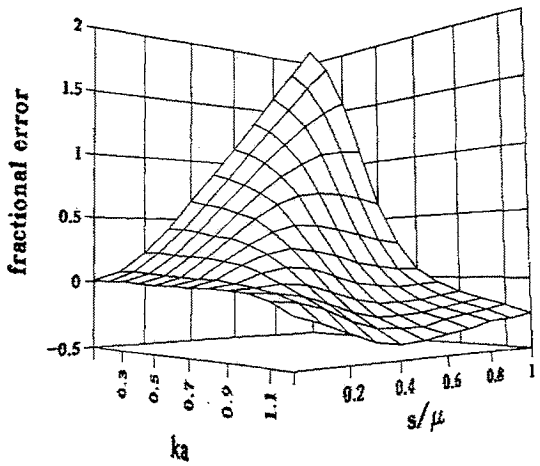

Fig.13 A plot of the predicted fractional error in scatterer size estimates (the bias error only) as a function of frequency (ka) and the breadth of the diameter distribution (s/μ). The F_2 model was used to estimate D. For $ka \simeq 0.8$, estimated size is predicted to equal the mean of the distribution with bias error less than 10 percent for $0 \leq s/\mu \leq 1$.

For this study, form factors were simulated by combining Eqs. (5), (6), and (11). F_1 model functions were used to compute each $\sigma_{b,i}$ in Eq. (11), and $\bar{\sigma}_b$ was used in place of σ_b in Eq. (6). The spherical shell model F_2 was then used to estimate D. For the simulations, the diameters were distributed about the mean value, μ, using a normal pdf with variance s^2. The variable that describes the distribution of diameters was the ratio of standard deviation to mean (s/μ). The fractional error that resulted is plotted versus ka and s/μ in figure 13. Since no noise has been introduced into the simulated data, the random error or variance is zero. The fractional error is entirely due to bias, which refers to the variation of the estimated D value about the mean of the distribution, *i.e.*, $(D-\mu)/\mu$. In figure 13, the value ka was determined by the mean diameter.

Strongly peaked distributions, *i.e.*, where $s/\mu \rightarrow 0$, gave the smallest error for all values of ka. In the Rayleigh scattering region, *i.e.*, where $ka \rightarrow 0$, D was overestimated by the factor

$$\left(\sum_{i=1}^{\infty} \frac{\bar{n}_i}{\bar{n}_T} D_i^6\right)^{1/6} \Big/ \left(\sum_{i=1}^{\infty} \frac{\bar{n}_i}{\bar{n}_T} D_i\right) \tag{12}$$

as predicted by Eq. (5). Consequently, D can be overestimated by more than 200 percent when $s/\mu = 1$ and $ka \rightarrow 0$. In general, as s/μ increases, we found that D is overestimated when ka is small and underestimated when ka is large. The most interesting finding is that the bias is less than 10 percent for all values of s/μ when $ka \simeq 0.8$. *This means that if the transducer frequency is chosen such that $ka \simeq 0.8$ for the mean of the distribution, then the measured D value will equal the mean of the size*

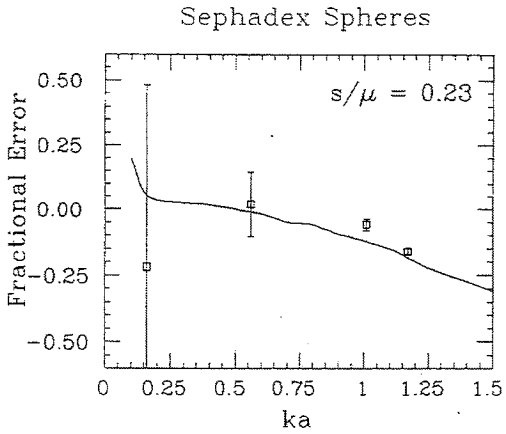

Fig.14 Verification of the predicted error in scatterer size measurements (Fig. 13) using Sephadex-in-agar test sample. In this sample, the standard deviation to mean ratio is 0.23. (See Fig. 4.) Error bars represent one standard deviation of the mean. Section 3.4.

distribution with a bias error less than 10 percent. Also, $ka = 0.8$ is at the center of the range of maximum measurement sensitivity for size measurements, *i.e.*, $0.5 \leq ka \leq 1.2$.

The predictions in figure 13 were verified experimentally using the Sephadex-in-agar samples described in Section 2.6 and figure 4. In the sample studied, $s/\mu = 0.23$. The predicted and measured errors are very similar as shown in figure 14. In addition to the bias, the measured values are subjected to random error, as reflected by the error bars. Twenty independent waveforms were used to compute an average spectrum for one D measurement, and each measurement was repeated eight times. The error bars in figure 14 denote the standard deviation of the mean D value for an average of eight measurements. This data demonstrates the loss of measurement sensitivity typical of measurements made at $ka < 0.5$. In this range, the noise in the spectral estimate is much greater than changes due to the size of the spheres.

4 DISCUSSION

The influence of the pulse frequency on the appearance of the scatterer size image was marked. Similarly, parameter estimation accuracy was also affected. The most important factor affecting the accuracy of the estimation, and therefore the appearance of the parametric image, was the accuracy of the correlation model, or equivalently the form factor over the measurement bandwidth. The chi-square image gave a very good indication of regions in the image where the correlation model broke down, *e.g.*, figure 8d. When viewed along with D and $\bar{n}\gamma_0^2$ images, the χ^2 image may be used to decide if a region stands out from the background because the parameters are different or because the correlation model used was inappropriate over the measurement bandwidth.

In the example of spherical scatterers, the form factor is an oscillating function of frequency. As a consequence, when the spectral estimates are noisy, there can be an ambiguity in the size estimate which appears as bright or dark spots throughout the image. (For example, see figures 10c and 10d.) Increasing the usable bandwidth more

uniquely identifies the measured spectrum, thereby reducing the ambiguity and image noise. However, the use of broader bandwidths requires more detailed prior information about the medium, *i.e.*, a very accurate correlation model, to obtain accurate parameter estimates. Therefore, before accurate estimation of scatterer size and strength in biological tissues is possible, the correlation functions for tissues must be measured. If it turns out that the form factors for tissues are not monotonically decreasing, as with the Gaussian model, but oscillate, as with a spherical or cylindrical model, then not only will the appearance of the image greatly depend on the transducer frequency and bandwidth, but a single type of scattering structure can appear as many different structures in the image depending on the noise in the spectrum.

Our method for computing the scattering strength from scatterer size estimates is ill-posed; it is an attempt to estimate two unknowns from one measurement [1]. As an alternative, we considered imaging backscatter coefficients at a specified frequency. The rationale is that even though D and σ_b images are more correlated than D and $\bar{n}\gamma_0^2$ estimates, σ_b estimates may be determined with greater accuracy and precision than $\bar{n}\gamma_0^2$ estimates. We found, however, that backscatter coefficients produced very noisy images, primarily because the uncertainty in σ_b estimates is related to the uncertainty of a single spectral value, rather than that of the entire bandwidth. As an alternative, we have generated *IBC* images which reduced the image noise by as much as 90 percent over σ_b images.

The similarity between *IBC* and B-mode images in figures 7 and 8 was expected. (B-mode images are labeled a; *IBC* images are labeled e.) The B-mode image displays the mean-square echo signal inside the range gate, and the *IBC* image displays the sum of backscatter coefficients, which are proportional to the power spectral density of the echo signal. The two images would be equivalent within a constant, as given by Rayleigh's theorem [9] , except that the system response has been eliminated from the *IBC* image data. Since data were acquired in the C-scan image plane, it is the lateral system response that is deconvolved from the echo signals in the *IBC* images. The net effect is to sharpen the target edges. Hence *IBC* images display the same information as B-mode images, but with greater spatial resolution. Scatterer size and strength images display the B-mode image information in two parts: D is determined from the frequency dependence of backscatter and $\bar{n}\gamma_0^2$ is determined from its magnitude. For example, the increased target brightness in figure 7 for the B-mode image (a) can be explained by a larger number of spheres in the targets (c and g), whereas in figure 8 the B-mode (a) target brightness can be explained by a larger average scatterer size (f).

5 SUMMARY AND CONCLUSIONS

It is possible to accurately estimate backscatter coefficients and image the average structural and elastic properties of media using commercially-avaliable real-time ultrasound instrumentation. An accurate correlation model and a large transducer bandwidth yield the most accurate estimates of scatterer size and strength. Large local variations in attenuation and inaccurate correlation models bias parameter estimates and the appearance of the image; for example, the polarity of low-contrast targets may vary with transducer frequency relative to the background. Chi-square images, however, can assist image interpretation by showing how well the data is represented by the correlation model. In general, selection of the center frequency of the transducer

primarily affects the bias error of the estimates — parametric image accuracy and contrast. Selection of the transducer bandwidth primarily affects the random error of the estimates — parametric image noise.

Size estimation accuracy is also influenced by the size distribution of scatterers in the medium. However, the center frequency of the transducer can be selected such that the estimated size and the mean of the distribution are equal within a 10 percent bias error. Therefore, it is not necessary to include the exact distribution of scatterer sizes in the correlation model to gain a meaningful interpretation of the results. Only normal probability distributions were considered in this study.

Based on these test sample measurements, we conclude that it can be difficult to interpret scatterer size and strength images in complex biological tissues without first obtaining accurate correlation models. Correlation models for tissue may be obtained using high-resolution acoustic microscopy. Since tissues are often acoustically heterogeneous and anisotropic, it seems likely that the most accurate correlation models will be functions of position and orientation within the tissue. An inaccurate model can lead to a false description of the underlying structure, as seen in figure 8. Spherical and cylindrical correlation models, which are oscillating functions of frequency, can yield ambiguous results, as demonstrated for spherical models in figure 10. However, under low-noise conditions and with broad-bandwidth systems, this ambiguity can be removed, as seen in figure 11. χ^2 images could become an important tool for developing correlation models for heterogeneous and anisotropic scattering media.

6 ACKNOWLEDGMENTS

The authors wish to thank H. H. Barrett from the University of Arizona for suggesting χ^2 imaging as a tool for correlation model evaluation, and R. J. Insana for her laboratory assistance. This project was supported in part by grants from The Whitaker Foundation and The National Institutes of Health, BRSG S07 RR05373.

References

[1] Insana, M.F., Wagner, R.F., Brown D.G., and Hall T.J., Describing small-scale structure in random media using pulse-echo ultrasound, *J. Acoust. Soc. Am. 87*, 179-192 (1990).

[2] Morse, P.M. and Ingard K.U., *Theoretical Acoustics*, (McGraw-Hill, New York, 1968).

[3] Chernov, L.A., *Wave Propagation in a Random Medium,* (McGraw-Hill, New York, 1960).

[4] Faran, J.J., Sound scattering by solid cylinders and spheres, *J. Acoust. Soc. Am. 23*, 405-418 (1951).

[5] Vaitkus, P.J., Cobbold, R.S.C., and Johnston, K.W., A comparative study and assessment of Doppler ultrasound spectral estimation techniques. Part II: methods and results, *Ultrasound Med. Biol. 14*, 673-688 (1988).

[6] Bevington, P.R., *Data Reduction and Error Analysis for the Physical Sciences,* Chapter 6, (McGraw-Hill, New York, 1969).

[7] Bendat, J.S. and Piersol, A.G., *Random Data Analysis and Measurement Procedures, 2nd ed.,* Section 10.5.3, (Wiley and Sons, New York, 1986).

[8] Thijssen, J.M., Oosterveld, B.J., and Wagner, R.F., Gray level transforms and lesion detectability in echogram images, *Ultrasonic Imaging 10,* 171-195 (1988).

[9] Bracewell, R.N., *The Fourier Transform and Its Applications, 2nd ed.,* (McGraw-Hill, New York, 1978.